ELSEVIER

Stability of gas pressure regulators

Naci Zafer [a,*], Greg R. Luecke [b,1]

[a] *Department of Mechanical Engineering, Eskisehir Osmangazi University, Makine Muhendisligi Bolumu,
26480 Bati Meselik, Eskisehir, Turkey*
[b] *Department of Mechanical Engineering, Iowa State University, Ames, IA 50010, USA*

Abstract

Gas pressure regulators are widely used in both commercial and residential applications to control the operational pressure of the gas. One common problem in these systems is the tendency for the regulating apparatus to vibrate in an unstable manner during operation. These vibrations tend to cause an auditory hum in the unit, which may cause fatigue damage and failure if left unchecked. This work investigates the stability characteristics of a specific type of hardware and shows the cause of the vibration and possible design modifications that eliminate the unstable vibration modes. A dynamic model of a typical pressure regulator is developed, and a linearized model is then used to investigate the sensitivity of the most important governing parameters. The values of the design parameters are optimized using root locus techniques, and the design trade-offs are discussed.
© 2006 Elsevier Inc. All rights reserved.

Keywords: Dynamics; Modeling; Stability; Vibrations; Pressure regulator

1. Introduction

Gas regulators are devices that maintain constant output pressure regardless of the variations in the input pressure or the output flow. They range from simple, single-stage [1,2] to more complex, multi-stage [3,4], but the principle of operation [5] is the same in all. High pressure gas flows through an orifice in the valve and the pressure energy in the gas is converted to heat and flow at the lower, regulated, pressure. The orifice faces a movable disk that regulates the amount of gas flow. A flexible diaphragm is attached to the disk by means of a mechanical linkage. The diaphragm covers a chamber such that one side of the diaphragm is exposed to atmospheric pressure and the other is exposed to the regulated pressure. When the regulated pressure is too high, the diaphragm and linkage move the disk to close the orifice. When the regulated pressure is too low, the disk is moved to open the orifice and allow more gas pressure and flow into the regulator. On the opposite side of the diaphragm, an upper chamber houses a wire coil spring and a calibration screw. The screw compresses the

* Corresponding author. Tel.: +90 222 239 3750x3387; fax: +90 222 239 3613/229 0535.
E-mail addresses: nzafer@ogu.edu.tr (N. Zafer), grluecke@iastate.edu (G.R. Luecke).
[1] Tel.: +1 515 294 5916; fax: +1 515 294 3261.

spring, which changes the steady state force on the diaphragm, allowing for the adjustment of the regulated pressure set point. If the regulated gas pressure rises above the safe operational pressure, an internal relief valve is opened to vent the excess gas through the upper chamber and into the atmosphere to prevent the danger of high pressure gas at the regulator outlet.

Little information is published regarding these devices, due to concerns over proprietary information. One reported study concerning high-pressure regulators is done by Kakulka et al. [6]. The regulator studied was a piston pressure-sensing unit that had a conical poppet valve that regulates the gas flow. The dynamic effects of restrictive orifices and the upstream and downstream volumes were addressed in the modeling and analysis. However, the source of the oscillations in the downstream exiting area, as well as the damping and the friction effects in the physical system, were left out. Several researchers have, on the other hand, addressed the unwanted oscillations and noise. Waxman et al. [7] eliminates the noisy oscillations with the implementation of a dead-band achieved by two micro switches. The design includes a stepping motor activated with the signal from a differential pressure transducer. Baumann [8] proposes a much less expensive solution, the use of a static pressure reducing plate with multiple holes. Ng [9] compares the effectiveness and cost of several methods that reduce or minimize the noise. Ng [10] addresses pressure regulators for liquids and names cavitations, the damage caused by continuous formation and collapse of microscopic bubbles, to be the cause of hydrodynamic noise. Cavitations produce noise, vibration, and even cause significant damage. Ng states that the use of quiet valves, or an orifice with multiple holes are not the solutions to this problem, since they are expensive and the small passages are most likely to be plugged by solid particles in the flow. Dyck [11] states that a larger restrictive orifice improves flow performance, but a small one makes the system more stable and is less sensitive to downstream pressure fluctuations. Liptak [12] gives an equation for the offset in the regulated pressure with changing flow and shows that any decrease in this offset pressure decreases the stability of the regulator, resulting in a noisy regulator with oscillatory pressure cycling. To stabilize the system he suggests using larger downstream pipe, a more restrictive flow from orifice to the lower chamber, straight lengths of pipe upstream and downstream. He also points out that maintaining gas flow at less than sonic velocities and eliminating changes in flow directions would reduce the noise. It is obvious that these changes are very restrictive from the design and installation perspective, and are not guaranteed to stabilize the system.

In this study, we develop a comprehensive dynamical model for a gas pressure regulator from first principles in order to gain a better understanding of its behavior. We first model an existing regulator and use empirical data as necessary to identify parameter values for the model. Using a linearized version of this model, we investigate the effects of parameter variations using classical root-locus techniques. Our motivation is to design a tool that allows for the identification of the most influential system parameters on the stability of the system, and to allow an assessment of any effects that changes in these parameters have on stabilization of the regulator.

A schematic diagram of a typical gas pressure regulator (American Meter Gas Regulator, Model 1800) is shown in Fig. 1. High pressure gas flows through an inlet orifice that is opened or closed by a disk and linkage
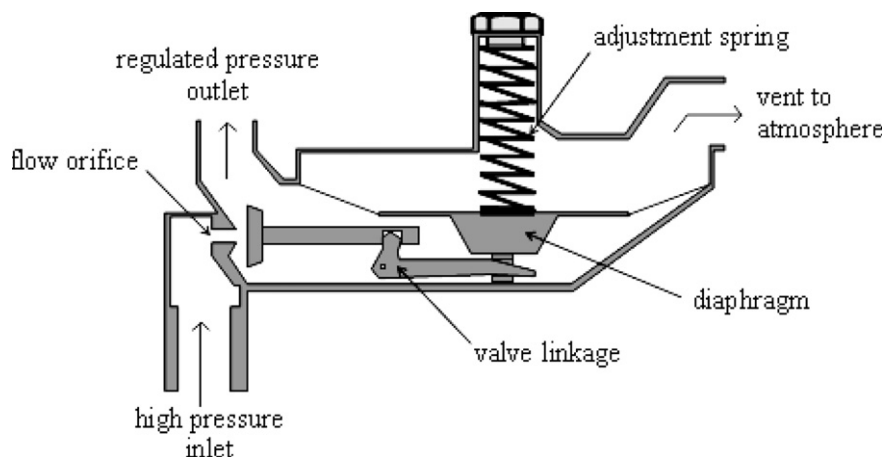

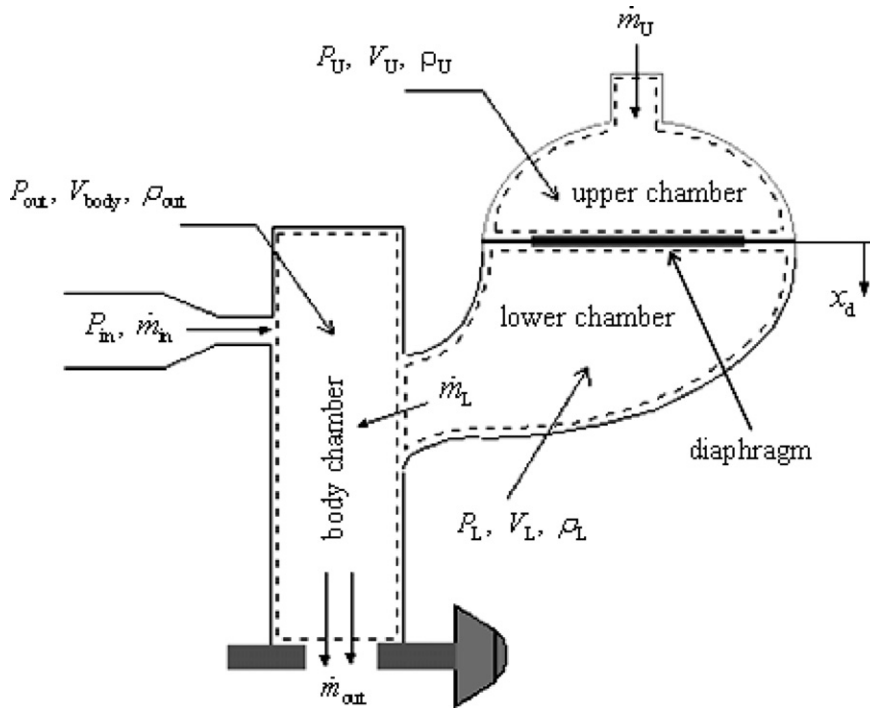Fig. 1. Operational diagram of a typical gas pressure regulator.

Fig. 2. Pressure regulator schematic.

attached to a diaphragm. The diaphragm moves in response to the balance between pressure inside the regulator body and the adjustment spring force. As the regulated pressure increases, the disk closes to restrict the incoming gas. When the regulated pressure is too low, the disk opens to allow more gas into the body cavity. The stability of the system depends on the amount of damping in the system, and much of the damping comes from flow restrictions within the regulator. In order to develop our model, we define three control volumes that are used in the dynamic analysis, identified in Fig. 2: the body chamber, the upper chamber and the lower chamber. Each control volume is characterized by pressure, volume, and the density as a function of time. For the purpose of this analysis, these control volumes are used to track the mass flow through the system.

2. Gas dynamics governing equations

Modeling of operation of the gas pressure regulator is based on the physical behavior of compressible fluid flow. The modeling in this work uses the fundamental principles of ideal compressible flow, the principle of conservation of mass, and well-known expressions for flow through orifices [13,14]. For the development of the pressure regulator model, we assume that the operating fluid is a perfect gas. Kinetic theory is then used to express the state of a particular control volume according to the ideal gas equation:

$$PV = mRT, \tag{1}$$

where P is the pressure, V is volume, m is mass, R is a gas constant, T is temperature. Assuming the process is adiabatic and reversible, the second law of thermodynamics provides a relationship between the pressure and the density of the fluid:

$$\frac{P}{\rho^k} = \text{Constant.} \tag{2}$$

By considering the time differentials of Eqs. (1) and (2) together with the definition of density, one can easily show that

$$\frac{1}{k}\frac{\dot{P}}{P} + \frac{\dot{V}}{V} = \frac{\dot{m}}{m},\tag{3}$$

where k is the specific heat ratio, and

$$\dot{m} = \rho Q, \quad m = \rho V.\tag{4}$$

Because the density for a fixed operational flow rate is constant, volumetric flow rate will be used, rather than the more conventional mass flow rate. Eq. (3) provides a basis for analysis and modeling of the pressure regulator and describes the relationship between pressure, volume, and the mass flow for a particular control volume.

2.1. Lower chamber

Applying Eqs. (3) and (4) to the lower chamber, we get

$$\frac{1}{k_{\mathrm{L}}}\frac{\dot{P}_{\mathrm{L}}}{P_{\mathrm{L}}} + \frac{\dot{V}_{\mathrm{L}}}{V_{\mathrm{L}}} = -\frac{Q_{\mathrm{L}}}{V_{\mathrm{L}}}.$$

Note that the minus sign indicates that our convention of the direction of positive flow, Q_{L}, is out of the cavity. The motion of the diaphragm is related to change in volume by

$$\dot{V}_{\mathrm{L}} = -\dot{x}_{\mathrm{d}}A_{\mathrm{d}},$$

where $\dot{x}_{\mathrm{d}}$ and A_{d} are the velocity and the surface area of the diaphragm. Because of the sign convention chosen for the diaphragm motion, a positive change in the diaphragm position causes the lower chamber volume to decrease. Although A_{d} has a nonlinear relationship with x_{d}, it is assumed constant for linear simulations. This assumption can be made because the operational inlet flow rates are, in general, small, less than 0.01 m^3 s^{-1}, and the diaphragm travel also remains relatively small for these flow rates. For the nonlinear simulations, the more accurate empirical relationship shown in Fig. 3 is used.

The overall equation governing the pressure–flow relationship in the lower chamber is then

$$\dot{P}_{\mathrm{L}} = k_{\mathrm{L}}\frac{P_{\mathrm{L}}}{V_{\mathrm{L}}}(-Q_{\mathrm{L}} + \dot{x}_{\mathrm{d}}A_{\mathrm{d}}).\tag{5}$$

Linearizing this equation using a Taylor series expansion and neglecting the higher order terms, we have:

$$\widetilde{\dot{P}}_{\mathrm{L}} = k_{\mathrm{L}}\frac{P_{\mathrm{L}0}}{V_{\mathrm{L}0}}(-\widetilde{Q}_{\mathrm{L}} + \widetilde{\dot{x}}_{\mathrm{d}}A_{\mathrm{d}}),\tag{6}$$

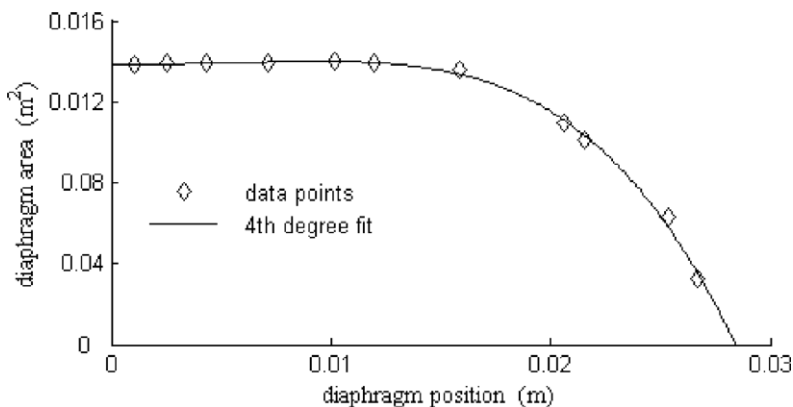where the notation "~" is used to express an incremental change of the related quantity.

Fig. 3. Empirical data for diaphragm travel vs. diaphragm area.

2.2. Upper chamber

A similar analysis for the upper chamber yields the differential equation governing the change in the pressure of the upper chamber:

$$\frac{1}{k_U}\frac{\dot{P}_U}{P_U} + \frac{\dot{V}_U}{V_U} = \frac{Q_U}{V_U},$$

where $\dot{V}_U = \dot{x}_d A_d$. The overall equation governing the pressure–flow in the upper chamber and the linearized form are then

$$\dot{P}_U = k_U \frac{P_U}{V_U}(Q_U - \dot{x}_d A_d), \tag{7}$$

$$\dot{\widetilde{P}}_U = k_U \frac{P_{U0}}{V_{U0}}(\widetilde{Q}_U - \dot{\widetilde{x}}_d A_d). \tag{8}$$

2.3. Body chamber

Although the flow out of the regulator is not steady, the gas pressure in the connected lower chamber and body chamber cavities fluctuates as the regulator moves to equilibrium. For a compressible gas, these fluctuations also compress the gas and change the density of the fluid. However, the changes in density in these chambers is small compared with the change density as the fluid moves from the high-pressure inlet to the lower pressure, regulated, body pressure. We can account for this change in density with an expansion ratio. Solving Eq. (3) for the body chamber using the outlet pressure gives:

$$\frac{1}{k_{out}}\frac{\dot{P}_{out}}{P_{out}} = \frac{\dot{m}_{body}}{m_{body}}.$$

Note that there is no change in volume for the body chamber, so that $\dot{V}_{body} = 0$ and the mass balance for the body chamber in Fig. 1 is obtained by summing the mass flow rates in and out of this chamber.

$$\dot{m}_{body} = \dot{m}_{in} - \dot{m}_{out} + \dot{m}_L.$$

Substituting $\dot{m} = \rho Q$ in this equation for each of the control volumes, it follows that

$$Q_{body} = \kappa Q_{in} - Q_{out} + Q_L,$$

where Q_{in} is the inlet flow-rate, and the expansion ratio

$$\kappa = \frac{\rho_{in}}{\rho_{body}}$$

is used to account for the change in density of the inlet gas to that of the outlet gas. Again, note that $\rho_{body} = \rho_{out} = \rho_L$ is assumed because the differences in pressure are small compared to the difference in pressure between these and the inlet pressure. Combining these equations gives the outlet pressure as a function of the flow crossing the control boundary:

$$\frac{1}{k_{out}}\frac{\dot{P}_{out}}{P_{out}} = \frac{\kappa Q_{in} - Q_{out} + Q_L}{V_{body}},$$

$$\dot{P}_{out} = k_{out}\frac{P_{out}}{V_{body}}(\kappa Q_{in} - Q_{out} + Q_L). \tag{9}$$

Using a Taylor series expansion, we also obtain the linear, incremental, equation:

$$\dot{\widetilde{P}}_{out} = k_{out}\frac{P_{out0}}{V_{body0}}(\kappa \widetilde{Q}_{in} - \widetilde{Q}_{out} + \widetilde{Q}_L). \tag{10}$$

2.4. Flow governing equations

Fluid enters and exits the gas regulator through three flow holes, the inlet valve, the outlet orifice, and through the relief valve on the top of the upper chamber, each of these flow components contributes to the dynamic response characteristics of the overall regulator.

Because the pressure drop is very large from the inlet pressure through the orifice, the sonic, or critical, flow into the regulator is proportional to the throat area [16], or the plunger travel. This provides a linear relationship between the flow into the regulator and the effective flow area between the orifice and the disk. This effective area is dependent on the annular distance between the face of the disk and the orifice and the specific geometry of both the disk and orifice, but is more or less constant in a specific valve.

$$Q_{in} = C_{in}x_p, \tag{11}$$

where the constant C_{in} is obtained from empirical data shown in Fig. 4. This equation is already linear, and the incremental representation is:

$$\widetilde{Q}_{in} = C_{in}\tilde{x}_p. \tag{12}$$

Flow in or out of the upper chamber occurs through a relief cap with a small vent hole. Generally, the upper chamber relief cap ventilation hole regulates flow during smaller adjustments of the diaphragm, and a spring-loaded relief plate prevents pressure build-up during large diaphragm motions or in the event of a rupture of the diaphragm. Using the assumption of a small orifice area when compared to the upper chamber cross sectional area, the flow through the ventilation hole in the upper chamber is expressed with the well-known square root relationship

$$Q_U = -C_{Ut}\sqrt{P_U - P_{atm}}, \tag{13}$$

where C_{Ut} is the nonlinear flow coefficient. With P_{atm} assumed constant, this equation is linearized using Taylor series expansion to yield

$$\widetilde{Q}_U = -C_U\widetilde{P}_U, \tag{14}$$

with $C_U = \frac{C_{Ut}}{2\sqrt{P_{U0} - P_{atm}}}$.

Note that for values of P_U close to the atmospheric pressure, or $\widetilde{P}_U$ close to zero, the linearized flow coefficient C_U gets large and leads to large flows in response to small pressure changes to maintain the equilibrium conditions. Theoretically, this square-root relationship leads to an infinite slope of the pressure–flow curve, and this is borne out by the experimental data for flow through the upper chamber orifice at various pressure differences, shown in Fig. 5. However, as the pressure difference gets very small, this theoretical square-root
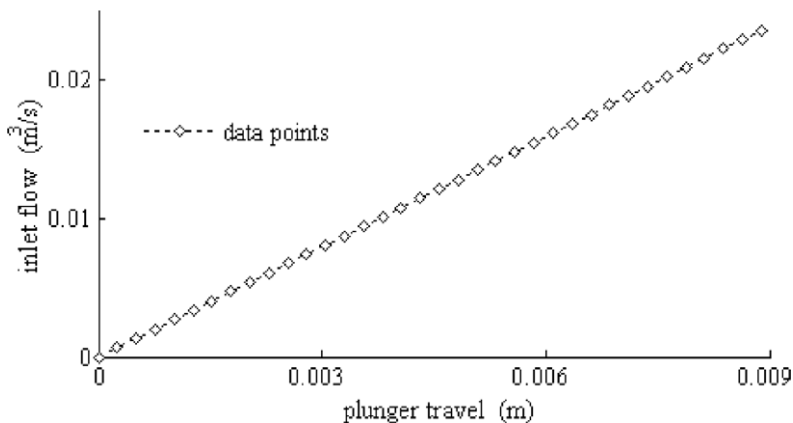

Fig. 4. Empirical data defining flow into the regulator as a function of the plunger travel.
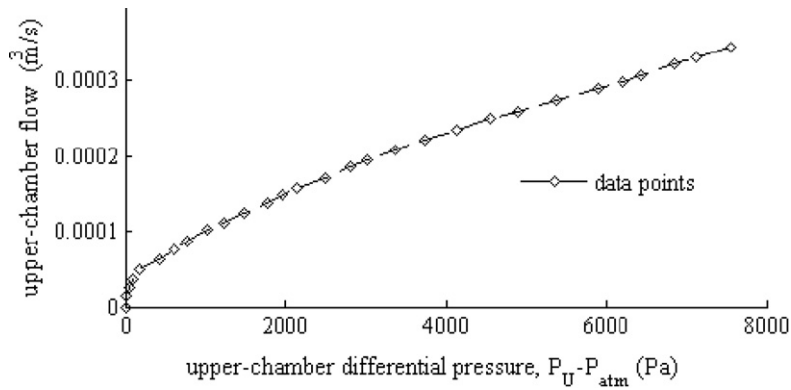
Fig. 5. Empirical data for the upper chamber defining pressure as a function of the flow.

relationship breaks down and leads to a linear relationship with a very high gain. For the modeling in this work, the empirical data depicted in Fig. 5 is used to get the flow coefficient for the nonlinear square-root model, C_{Ut}. For the linear model, C_U is the slope of the curve in Fig. 5, and with low flow rates, C_U will be very large.

Flow out of the regulator is modeled using the assumption that the outlet orifice area is variable, which affects the gas pressure in the regulator body. This approach assumes that the flow demand to the regulator is not separated from the body by additional dynamics from subsequent piping, and that the changes in flow demand can be modeled as a variable orifice area at the regulator outlet. Using this approach, the flow out of the orifice is:

$$Q_{out} = AC_d\sqrt{P_{out} - P_{atm}}, \tag{15}$$

where "A" represents the variable area or demand from downstream. Linearization of this flow relationship about an equilibrium state has a slightly different result, because the pressure difference between the outlet and the atmosphere never goes to zero. The outlet flow is a function of two variables, the pressure drop, $(P_{out} - P_{atm})$, and the flow area, A. This linearization leads to

$$Q_{out} = Q_{out0} + \frac{\partial\left(AC_d\sqrt{P_{out} - P_{atm}}\right)}{\partial A}\Bigg|_{\substack{P_{out}=P_{out0}\\A=A_0}}(A - A_0) + \frac{\partial\left(AC_d\sqrt{P_{out} - P_{atm}}\right)}{\partial P_{out}}\Bigg|_{\substack{P_{out}=P_{out0}\\A=A_0}}(P_{out} - P_{out0})$$

or

$$\widetilde{Q}_{out} = C_{10}\widetilde{A} + C_{20}\widetilde{P}_{out}, \tag{16}$$

where $C_{10} = \frac{Q_{out0}}{A_0}$, $C_{20} = \frac{A_0^2 C_d^2}{2Q_{out0}}$. While we continue to use empirical data to find typical value for the discharge coefficient, C_d, in Eq. (15), for a given equilibrium condition the linear model uses the constant coefficients in Eq. (16).

The flow into and out of the lower chamber is a complex function of the flow of gas through the regulator and the shape of the flow cavity. The classical square-root relationship shown in Eq. (15) does not do a good job of describing the pressure–flow relationships found for regulators experimentally. Fig. 6 shows a typical relationship for the lower chamber and body chamber pressures at various steady state flow conditions. This data indicates that the lower chamber pressure is lower than the outlet pressure in the body of the regulator. This is known as the "boost effect" and is caused by the venturi effect of the dynamic flow through the valve body. In practice, this boost effect is carefully designed into the regulator as a means of obtaining constant regulation pressure over a wide range of flows, but using a model such as that in Eq. (15) means that there should always be flow from the lower chamber into the body. Since the lower chamber is a fixed volume at steady state flow, this clearly cannot happen. Multiple flow paths, the dynamics of the fluid, and the geometry of internal obstructions make it difficult to develop an effective analytic model, but one approach is to imagine
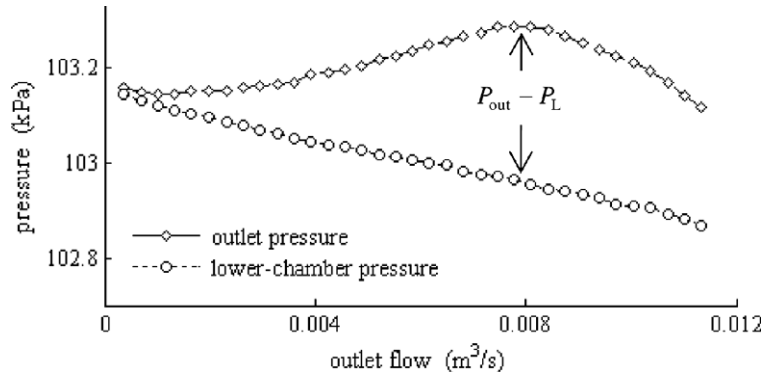
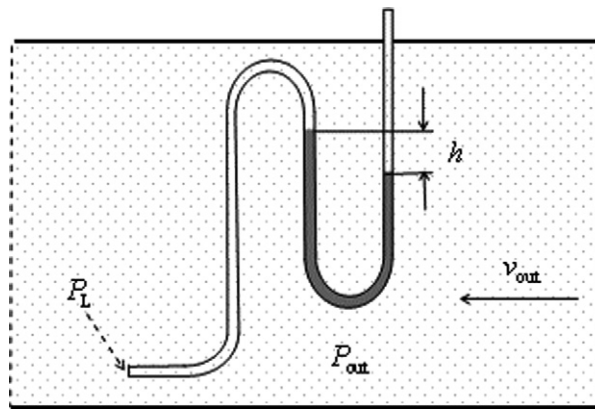Fig. 6. Empirical pressure and flow relationships.

Fig. 7. Reversed pitot tube.

a reversed pitot tube as shown in Fig. 7, where the tube is oriented to face downstream to allow measurement of the venturi effect of the moving fluid. The static pressure head (the effective lower chamber pressure), measured at P_L is found using Bernoulli's equation:

$$P_L^* = P_L + 0.5\rho_{out}v_{out}^2 = P_L + \frac{\rho_{out}}{2A_m^2}Q_{out}^2, \tag{17}$$

where A_m is the outlet orifice effective area, and P_L is the measured pressure inside the lower chamber (which is also the pressure inside the tube in Fig. 7).

At steady state, the pressure difference, $P_L^* - P_{out}$, should be zero, since there is no flow in or out of the closed lower chamber, and we can use the experimental test data in Fig. 6 to compute the effective coefficient on the last term in Eq. (17):

$$P_L^* = P_{out} \Rightarrow P_{out} - P_L = P_L^* - P_L = \frac{\rho_{out}}{2A_m^2}Q_{out}^2.$$

The pressure difference from Fig. 6, $P_{out} - P_L$, should be proportional to the square of the flow, and from Fig. 8a, the empirical data for lower flow rates shows that the effective venturi coefficient is:

$$\frac{\rho_{out}}{2A_m^2} = 5.6 \times 10^6.$$

Natural gas is mostly methane, and the density at atmospheric pressures is approximately 0.7 kg/m³. Using this density leads to an effective outlet area of $A_m = 2.5 \times 10^{-4}$ m³.
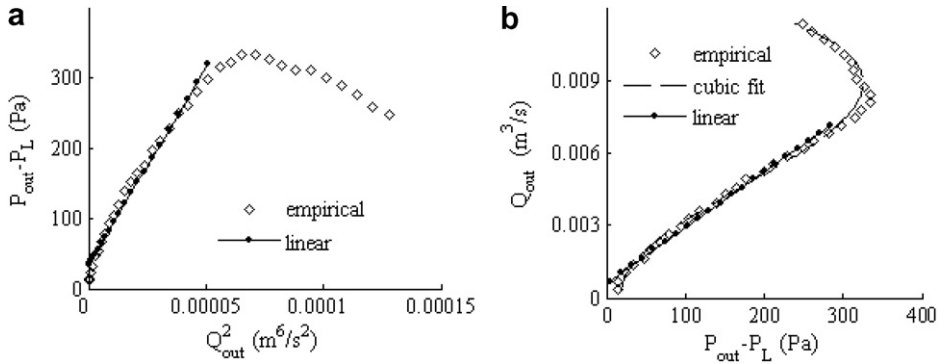
Fig. 8. Pressure difference between lower chamber and body chamber for various flow rates.

In our model, we used a maximum 3/4 in. (0.019 m) diameter outlet orifice (hardware outlet diameter) and for this the actual area is 2.8502×10^{-4} m^3. Although the flow path for the actual body chamber is more complex than any standard nozzle, it is well understood that flow though an orifice generates a *vena contracta* such that the effective flow area is smaller than the actual hole size. Comparing the flow area from the test data with the actual hardware hole size indicates that we need to use a coefficient for the area contraction of 0.877. This value for the flow coefficient due to the effect of *vena contracta* corresponds well to typical published values between 0.73 and 0.97, depending on the shape of the opening [17].

For our linear model, Eq. (17) becomes

$$\widetilde{P}_L^* = \widetilde{P}_L + \frac{\widetilde{Q}_{out}}{K_L} \tag{18}$$

with $K_L = \frac{A_m^2}{\rho_{out} Q_{out0}}$, representing the boost factor. Fig. 8b shows the experimental pressure difference along with a linear least-fit approximation of the constant, K_L leading to 2.3×10^{-5}.

Also shown in Fig. 8b is a cubic least-square regression for the effective pressure that is used in the full non-linear model. Note that the linear approximation compares favorably with the nonlinear experimental data up to about 0.007 m^3 s^{-1}. In simulation, this model of the boost effect resulted in a satisfactory response for both the linear model and the nonlinear model at both low and moderate flow rates (as illustrated later in Section 3). At very high flow rates, the venturi effect begins to fall off, and for the nonlinear model a cubic regression is used to develop a more accurate representation of the pressure–flow relationship. This polynomial has been implemented as the function for P_L^*, the fictitious equivalent pressure of the lower chamber:

$$P_L^* = P_L + f(Q_{out}). \tag{19}$$

The resulting model output for steady state conditions is shown for both the linear model and the nonlinear models in Fig. 8b. Using this effective pressure in the lower chamber, the flow between the body and the lower chamber is then

$$Q_L = C_{dL} \sqrt{P_L^* - P_{out}}. \tag{20}$$

In order to determine the flow coefficient, a test was performed by removing the diaphragm and pumping air from the lower chamber and out through the valve body. This data is shown in Fig. 9a for flow from the lower chamber to the valve body chamber for a particular valve, and this substantiates the use of Eq. (19) in the model. The data was taken by removing the diaphragm and just flowing air from the lower chamber out of the body, with no venturi effects. The discharge coefficient for Eq. (20) was found by plotting $(P_L - P_{out})$ vs. Q_L^2, as shown in Fig. 9b, and finding the square root of the slope. The value of the nonlinear discharge coefficient used in simulations is $C_{dL} = 5.5 \times 10^{-4}$.
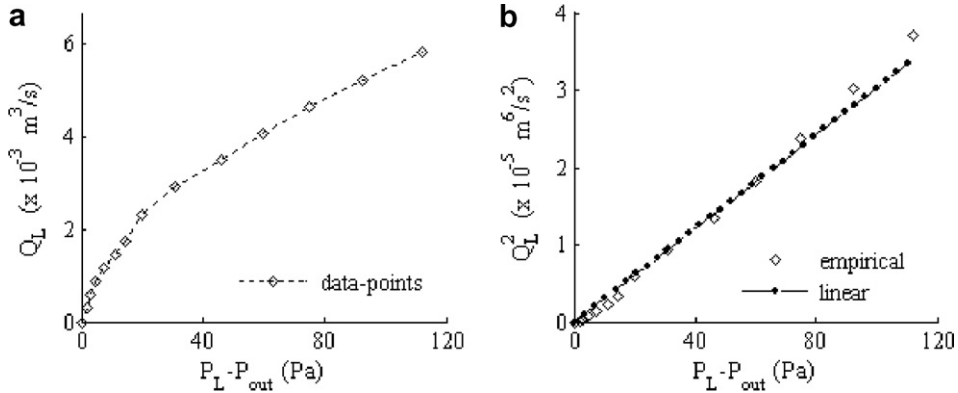
Fig. 9. Pressure–flow relationship between the lower chamber and the body chamber.

We can linearize Eq. (21) as

$$Q_L = Q_{L0} + \frac{\partial\left(C_{dL}\sqrt{P_L^* - P_{out}}\right)}{\partial P_L}\Bigg|_{\substack{P_L^* = P_{L0}^* \\ P_{out} = P_{out0}}} (P_L^* - P_{L0}^*) + \frac{\partial\left(AC_d\sqrt{P_L^* - P_{out}}\right)}{\partial P_{out}}\Bigg|_{\substack{P_L^* = P_{L0}^* \\ P_{out} = P_{out0}}} (P_{out} - P_{out0}) + \text{h.o.t},$$

$$\approx Q_{L0} + \frac{1}{2C_{dL}\sqrt{P_{L0}^* - P_{out0}}}\left[(P_L^* - P_{L0}^*) - (P_{out} - P_{out0})\right].$$

Defining $C_L = \frac{1}{2C_{dL}\sqrt{P_{L0}^* - P_{out0}}}$ and using $\widetilde{P}^*_L = \widetilde{P}_L + \frac{\widetilde{Q}_{out}}{K_L}$, we develop a linear flow model for lower chamber:

$$\widetilde{Q}_L = C_L(\widetilde{P}^*_L - \widetilde{P}_{out}) = C_L\left(\widetilde{P}_L + \frac{\widetilde{Q}_{out}}{K_L} - \widetilde{P}_{out}\right). \tag{21}$$

The linearized discharge coefficient, C_L, is slope of the line in Fig. 9a at the particular flow rate of interest.

2.5. Mechanical system governing equations

The mechanical parts of the system also contribute to the dynamic response of the system. The gas pressure regulator is represented with a simplified model as shown in Fig. 10. Free body diagrams are given in Fig. 11. A simple dynamic analysis of the free body diagrams leads to
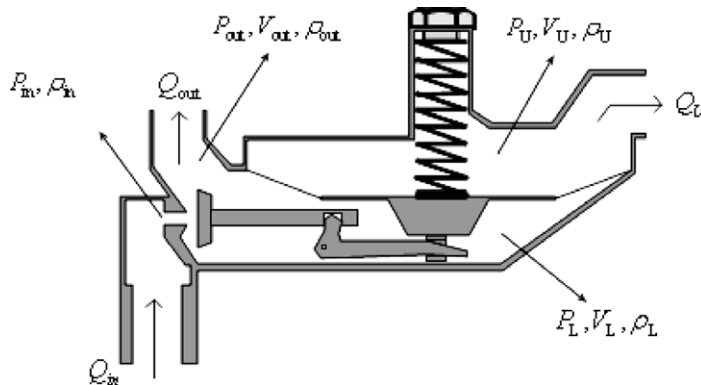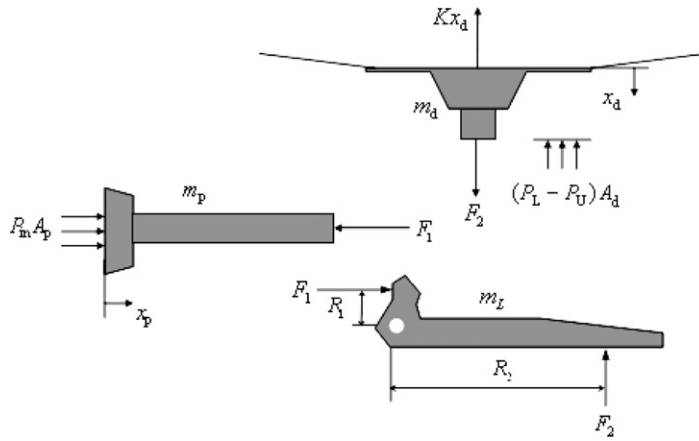

Fig. 10. Pressure regulator.

Fig. 11. Free body diagrams.

$$M\ddot{x}_d + b\dot{x}_d + Kx_d + A_d(P_L - P_U) = P_{in}A_p/L, \tag{22}$$

$$M\ddot{\widetilde{x}}_d + b\dot{\widetilde{x}}_d + K\widetilde{x}_d + A_d(\widetilde{P}_L - \widetilde{P}_U) = 0, \tag{23}$$

where the equivalent system mass is a combination of the mass of each part

$$M = \frac{J_L}{R_2^2} + \frac{m_p}{L^2} + m_d + \frac{m_s}{3}.$$

Here we have used the traditional analysis for the effective mass of a spring, based on the concept of conservation of total energy in the spring [15], even though this is likely a negligible component of the total inertia. Because we make an assumption that the mechanical linkage shown in Fig. 10 is rigid, the inertia and damping are reflected by the square of the motion ratios, where $L = R_2/R_1$. Note that the diaphragm and the plunger displacements are related by $x_d = Lx_p$ and that the effect of any flow forces on the plunger has been neglected.

3. Dynamic system response

The mechanical and fluid equations developed in the previous sections are used to simulate the operation of the gas regulator. Combining the incremental equations (6), (8), (10) and (23) together with Eqs. (12), (14), (16) and (21) to express the system as a set of dependent differential equations at a steady state operating point, we obtain the four governing equations for the system;

$$\dot{\widetilde{P}}_L = k_L \frac{P_{L0}}{V_{L0}} \left[-C_L \widetilde{P}_L - \frac{C_L C_{10}}{K_L} \widetilde{A} + C_L \left(1 - \frac{C_{20}}{K_L} \right) \widetilde{P}_{out} + \dot{\widetilde{x}}_d A_d \right],$$

$$\dot{\widetilde{P}}_U = k_U \frac{P_{U0}}{V_{U0}} (-C_U \widetilde{P}_U - \dot{\widetilde{x}}_d A_d),$$

$$\dot{\widetilde{P}}_{out} = k_{out} \frac{P_{out0}}{V_{body0}} \left[\kappa \frac{C_{in}}{L} \dot{\widetilde{x}}_d + \left(\frac{C_L C_{10}}{K_L} - C_{10} \right) \widetilde{A} + \left(\frac{C_L C_{20}}{K_L} - C_{20} - C_L \right) \widetilde{P}_{out} + C_L \widetilde{P}_L \right],$$

$$M\ddot{\widetilde{x}}_d + b\dot{\widetilde{x}}_d + K\widetilde{x}_d + A_d(\widetilde{P}_L - \widetilde{P}_U) = 0.$$

These equations are also illustrated by the block diagram shown in Fig. 12. The numbers in parenthesis in the figure correspond to equation numbers in the text.

For the nonlinear model, four independent equations govern the dynamics of the system. These equations are obtained by combining Eqs. (5), (7), (9) and (22) together with Eqs. (11), (13), (15) and (20);
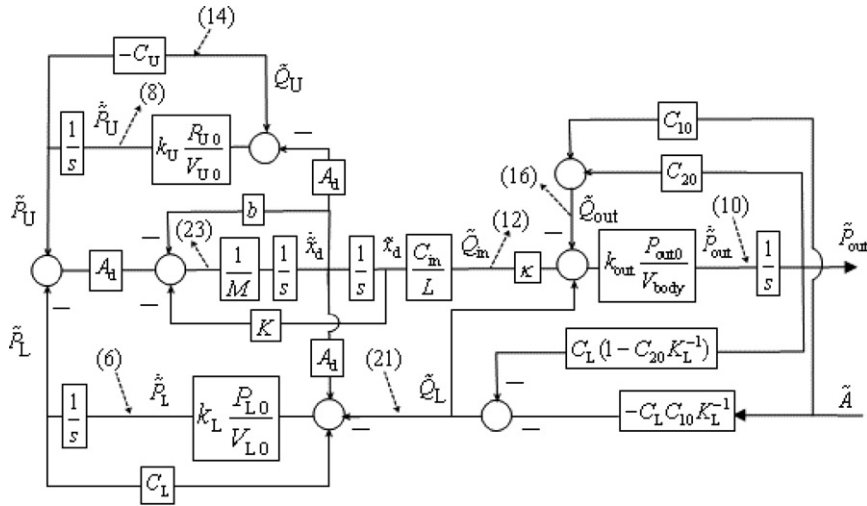
Fig. 12. System block diagram.

$$\dot{P}_{\mathrm{L}} = k_{\mathrm{L}} \frac{P_{\mathrm{L}}}{V_{\mathrm{L}}} \left(\dot{x}_{\mathrm{d}} A_{\mathrm{d}} - C_{\mathrm{dL}} \sqrt{P_{\mathrm{L}}^* - P_{\mathrm{out}}} \right),$$

$$\dot{P}_{\mathrm{U}} = -k_{\mathrm{U}} \frac{P_{\mathrm{U}}}{V_{\mathrm{U}}} \left(\dot{x}_{\mathrm{d}} A_{\mathrm{d}} + C_{\mathrm{Ut}} \sqrt{P_{\mathrm{U}} - P_{\mathrm{atm}}} \right),$$

$$\dot{P}_{\mathrm{out}} = k_{\mathrm{out}} \frac{P_{\mathrm{out}}}{V_{\mathrm{body}}} \left(\kappa \frac{C_{\mathrm{in}}}{L} x_{\mathrm{d}} - A C_{\mathrm{d}} \sqrt{P_{\mathrm{out}} - P_{\mathrm{atm}}} + C_{\mathrm{dL}} \sqrt{P_{\mathrm{L}}^* - P_{\mathrm{out}}} \right),$$

$$M \ddot{x}_{\mathrm{d}} + b \dot{x}_{\mathrm{d}} + K x_{\mathrm{d}} + A_{\mathrm{d}} (P_{\mathrm{L}} - P_{\mathrm{U}}) = P_{\mathrm{in}} A_{\mathrm{p}} / L + F_{\mathrm{c}}.$$

Here, P_{L}^* is the equivalent pressure of the lower chamber described by Eq. (17) for the pitot, or by Eq. (19) for the cubic fit approaches. Lower and upper chamber volumes may be approximated by $V_{\mathrm{L}} = V_{\mathrm{L0}} - A_{\mathrm{d}} x_{\mathrm{d}}$ and $V_{\mathrm{U}} = V_{\mathrm{U0}} + A_{\mathrm{d}} x_{\mathrm{d}}$, where initial diaphragm position is $x_{\mathrm{d0}} = \frac{L}{C_{\mathrm{in}}} Q_{\mathrm{in0}} = \frac{L}{C_{\mathrm{in}}} \frac{Q_{\mathrm{out0}}}{\rho_{\mathrm{NL}}}$ and A_{d} is a function of x_d described in Fig. 3. Because $x_{\mathrm{d0}} \neq 0$, a force to initially calibrate the regulator is required. This is done by adding the term $F_{\mathrm{c}} = K x_{\mathrm{d0}} + A_{\mathrm{d}} (P_{\mathrm{L0}} - P_{\mathrm{U0}}) - P_{\mathrm{in}} A_{\mathrm{p}} / L$ into the mechanical system equation.

The simulation is used to verify the basic operational characteristics of the system, including the time response and the stability of the regulator. The full nonlinear model is used to validate the overall operation of the regulator, including the transient response to large and small changes in outlet flow rates and steady state pressure and flow conditions. Our main objective is to show that the simulations operate in a reasonable way in response to normal inputs, and in a manner consistent with observed behavior of the physical gas regulator. Fig. 13 shows the simulation results for the steady state outlet pressure as a function of the outlet flow rate. The three modeling approaches are compared with the empirical data, and it is clear that there is a difference in the steady state response using the linear and nonlinear models, particularly at higher flow rates. Fig. 13 also shows the input values used to test the models: a small flow demand of 0.001 m³ s⁻¹ and larger demands of 0.0065, 0.0071, 0.0092 and 0.0098 m³ s⁻¹, along with the outlet orifice areas used to generate these flows. First, the linear model will be compared to the nonlinear simulations to show that the linear model is valid for small amplitude response about an equilibrium point. Next, using the linear model, we will apply the powerful root locus techniques to investigate the effects of changes in various parameters on the system response and stability.

Fig. 14 shows the time response of both the linear and the nonlinear models to a small step input in flow demand, corresponding to case I in Fig. 13. The initial outlet flow rate was set to $Q_{\mathrm{out0}} = 3.9329 \times 10^{-4}$ m³ s⁻¹ and the step change for the outlet orifice area was taken as $\tilde{A} = 1.5355 \times 10^{-5}$ m². Note that the sudden change in the outlet valve orifice area causes the pressure to drop, and then come back to the steady state. The sudden change first causes a drop in the regulated pressure, which is then restored as the plunger moves to a new steady state location. The small steady state errors are caused by the differences in the model assump-
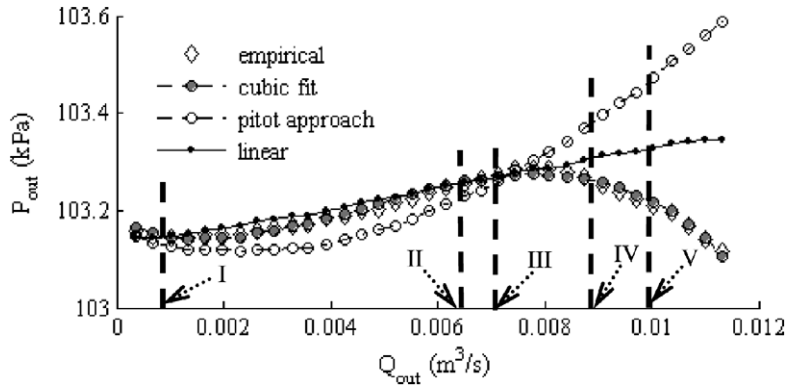
Fig. 13. Outlet pressure and flow relationships: (I) $A = 3.2258 \times 10^{-5}$ m^2; (II) $A = 2.7493 \times 10^{-4}$ m^2; (III) $A = 3.013 \times 10^{-4}$ m^2; (IV) $A = 3.93 \times 10^{-4}$ m^2; (V) $A = 4.2344 \times 10^{-4}$ m^2.
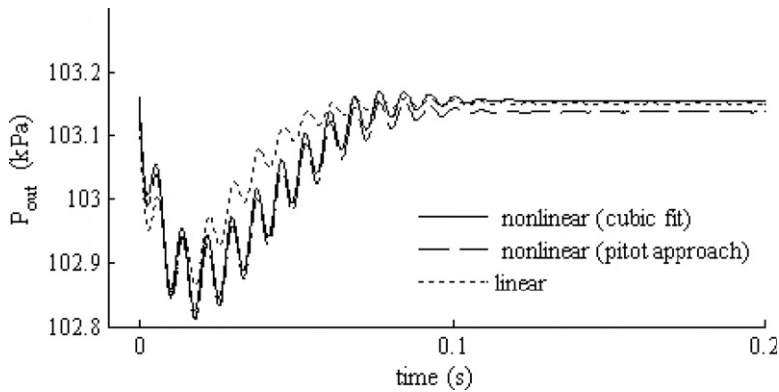

Fig. 14. Time response to step change in outlet area, $A = 3.2258 \times 10^{-5}$ m^2.

tions, and while there are differences in the amplitude of the oscillations, the frequencies and settling times match well.

Operational data for typical gas regulators show that the hardware has a tendency to exhibit dynamically unstable behavior under certain operating conditions. This instability causes the regulator to vibrate, or hum, although the gross operation of the regulator is not affected. Indeed, one major problem with this dynamic instability is that the causal observer may become alarmed by the noise, requiring replacement of the unstable regulator. One common factor of instability is the coupling of the upper chamber with a large volume discharge tube for venting purposes. While changes in many other factors, including temperature, flow, and atmospheric pressure, affect the unstable response, empirical evidence indicates that it is possible to tune this discharge volume to induce the unstable behavior regardless of other factors.

In order to establish the conditions for the regulator to hum, we studied the time response of the regulator with an upper chamber volume about four times larger than the nominal value of the actual hardware, $V_{U0} = 0.0025$ m^3, and the time response is shown in Fig. 15. This condition caused instability in both the non-linear and the linear model. The time response of both the linear and the nonlinear models at these large upper chamber initial volumes predict the frequency of oscillation at about <133 Hz. Fig. 15b also shows that the frequency is the same for both the linear and nonlinear models, although there is a phase difference between them. This phase difference is caused by a very small difference in frequency between the nonlinear models and the linear model, which adds up over many cycles. The small lag gets larger if the initial displacement from the equilibrium is made larger [18].

Fig. 16 shows the time response of the regulator models for large and small inputs at the intermediate flow rates of cases II and III in Fig. 13. In the center plot, there are two step changes in the flow demand, a large change at time = 0 corresponding to an initial outlet flow area of $A_0 = 1.6903 \times 10^{-5}$ m^2 and changing to
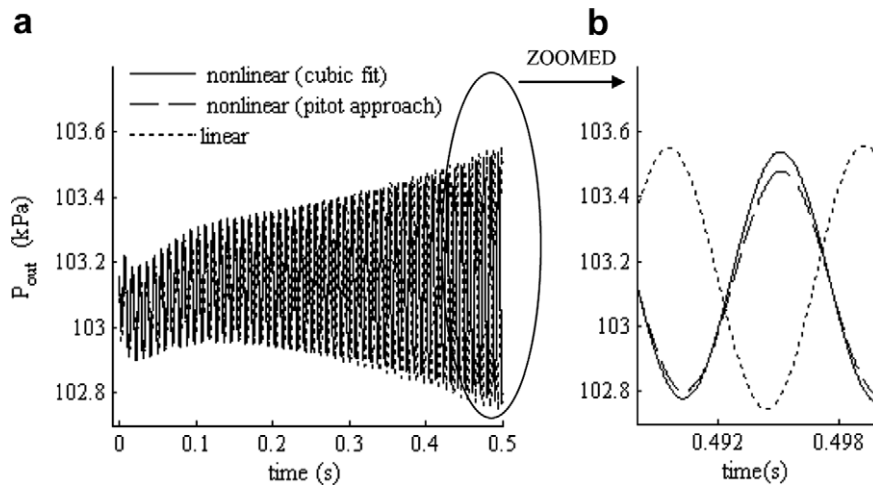
Fig. 15. Regulator response with large upper chamber volume, $A = 3.2258 \times 10^{-5}$ m^2.
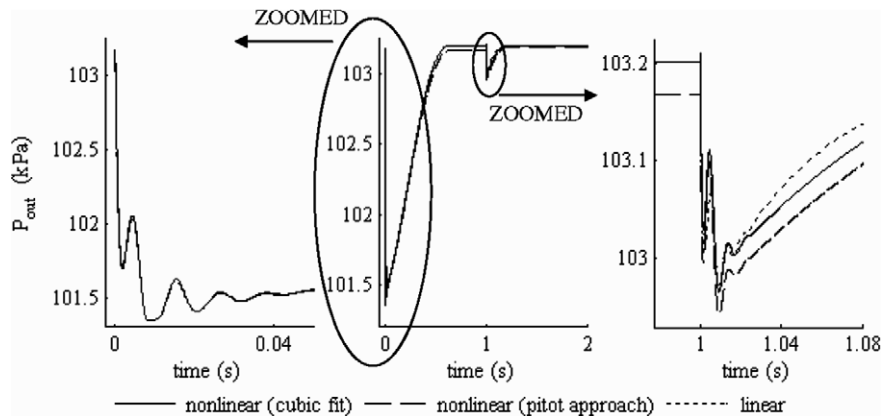

Fig. 16. Time response to step changes in outlet area, $V_{U0} = 6 \times 10^{-4}$ m^3 (nominal value).

$A = 2.7493 \times 10^{-4}$ m^2, and a small change at time $= 1.0$ corresponding to a change in outlet flow area from the steady state at $A_0 = 2.7493 \times 10^{-4}$ m^2 and changing to $A = 3.013 \times 10^{-4}$ m^2 thereafter. The flow rate settles to a steady state of $Q_{out} = 0.0065$ m^3 s^{-1} during the first second, and to $Q_{out} = 0.0071$ m^3 s^{-1} by the end of the simulation. Because the step change for the first second is quite large, only the nonlinear models are used in the simulation. Once the steady state is reached, the flow and pressure values are used to update the linear model parameters and the response of the linear and nonlinear models are compared for the small amplitude input, shown in the zoomed portion on the right of Fig. 16. Thus, both the nonlinear and the linear model are compared after the step at 1 s in the simulation. For small amplitude inputs, the linear model dynamics closely match the nonlinear model simulations, although there are steady state errors predicted by Fig. 13.

This same set of large and small inputs is shown in Fig. 17, but in this case, with a large upper chamber volume $V_{U0} = 6 \times 10^{-3}$ m^3. Again, the initial, large step input is only simulated using the nonlinear models, and the linear model is compared to the nonlinear responses for the small step input at 1.5 s. In this case, the linear model response still follows the nonlinear dynamics, although for both linear and nonlinear cases we see that the increase in the upper chamber volume has the effect of slowing the settling time of the regulator.

Fig. 18 shows the time response of the regulator for very high flow rates corresponding to cases IV and V from Fig. 13. These step changes in the outlet orifice area from $A_0 = 1.6903 \times 10^{-5}$ m^2 to $A = 3.93 \times 10^{-4}$ m^2 in the first 1 s and $A = 3.93 \times 10^{-4}$ m^2 to $A = 4.2344 \times 10^{-4}$ m^2 at 1.5 s correspond to steady state flow rates of $Q_{out} = 0.0092$ m^3 s^{-1} and to $Q_{out} = 0.0098$ m^3 s^{-1} respectively. Again, the steady state values of the nonlinear
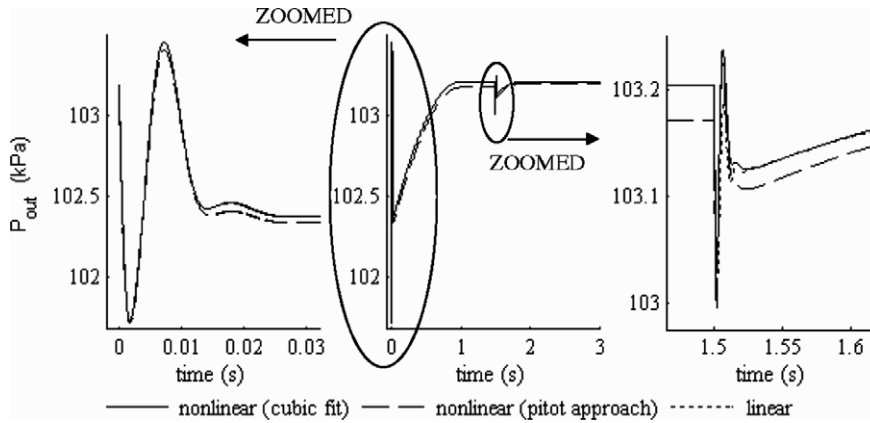
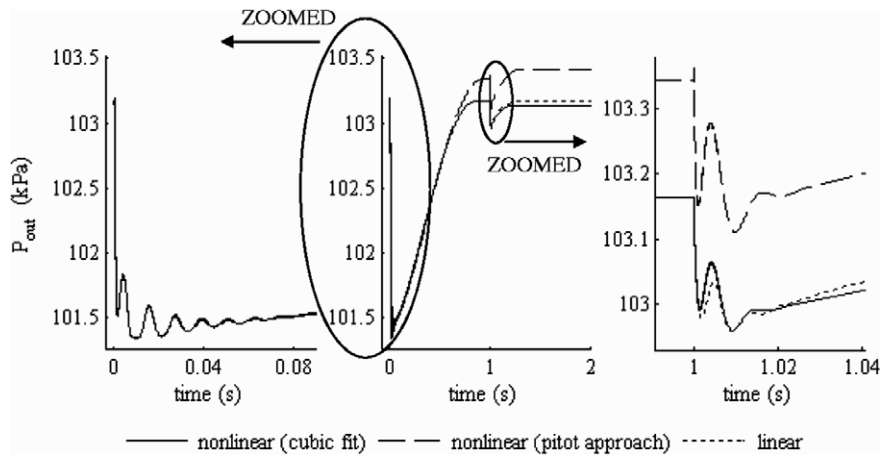Fig. 17. Time response to step changes in outlet area, $V_{U0} = 6 \times 10^{-3}$ m^3.

Fig. 18. Time response to step changes in outlet area, $V_{U0} = 6 \times 10^{-4}$ m^3 (nominal value).

model after the first large step input are used update the linear model parameters. Thus, both the nonlinear and the linear models are compared in the second part of the simulation, shown in the right of the figure. Note that during the initial response for the large step input, the system is very under damped, as shown by the oscillations in the left-hand portion of Fig. 18. For the smaller input at the higher flow rate, however, the dynamics show considerably more damping, indicating that higher flow rates tend to stabilize the system. Fig. 19 shows the response for this same set of inputs with the larger upper chamber volume, $V_{U0} = 6 \times 10^{-3}$ m^3. Here again, it is clear that the higher flow rates tend to stabilize the system response.

These simulations show that the mathematical models of the gas regulator produce reasonable response to changes in flow demands. The dynamic instability seen in real regulators for small flow rates can be reproduced in the simulations by increasing the upper chamber volume, which is also true for regulators in actual operation. The linear model closely matches the nonlinear model close to equilibrium positions and for small inputs. We will now use linear analysis methods to identify design parameters that have an effect on the stability of the system.

4. Linear system analysis

In order to understand the effects of various parameters on the stability of the system, an analysis of the linear system has been examined in the form of a root locus diagram for several parameters. This method
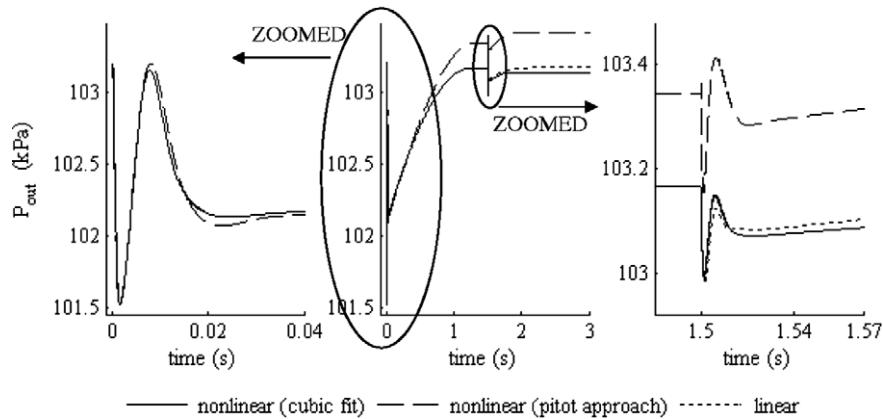
Fig. 19. Time response to step changes in outlet area, $V_{U0} = 6 \times 10^{-3}$ m^3.

allows for the determination of the effects on stability from changes in each model parameter separately. The root locus analysis was implemented for various design parameters that could be realistically modified to improve the stability of the regulator. These include the damping, b, the upper chamber volume, V_{U0}, the lower chamber volume, V_{L0}, the discharge coefficient between the upper chamber and the atmosphere, C_U, the discharge coefficient between the lower chamber and the body chamber, C_L, and the area of the diaphragm, A_d.

For the system with nominal parameter values, the system was stable, although there are roots close to the right half plane. The roots of the characteristic equation for the transfer function of the block diagram in Fig. 12 are -7306.4, $-27.7 \pm 801.9i$, $-62.7 \pm 41.1i$ when $V_{U0} = 6 \times 10^{-4}$ m^3, and -7306.3, -92.3, -21.9, $1.9 \pm 655.7i$ with $V_{U0} = 0.0025$ m^3.

We use the root locus for the linear model to investigate the effects of changes for various design parameter on system stability. The parameters chosen for investigation are those that can be realistically changed in the design of the regulator to improve stability. The nominal values used in the root locus come from the analytic development and incorporate measured values where possible, and are shown in Table 1.

4.1. Root locus on the damping coefficient

Increasing the mechanical damping in the system has the effect of stabilizing the system. This damping coefficient is very difficult to measure in the real hardware, and in our simulation, this value has been adjusted heuristically as a means of adjusting the system models to more closely match the experimental performance of the hardware. The adjustment of the damping coefficient, however, must be made within realistic limits. Fig. 20 shows a root locus plot for variable damping. There are two plots shown, one for a small upper chamber volume, V_{U0}, and one for a large upper chamber volume. While increasing the damping reduces the tendency toward unstable behavior, excessive increases in damping tends to increase the transient response time of the system, and lead to undesirable steady state effects such as dead-band.

Table 1
Nominal values of parameters used in the linear simulation

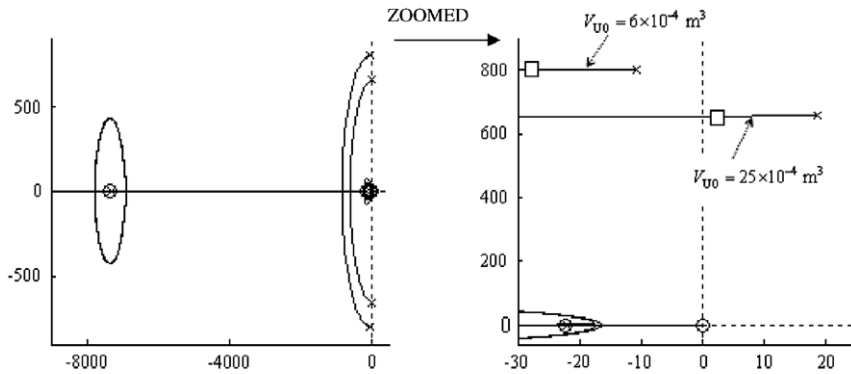|			
$A = 3.2258 \times 10^{-5}$ m^2	$A_0 = 1.6903 \times 10^{-5}$ m^2	$A_d = 0.0139$ m^2	$A_m = 2.5 \times 10^{-4}$ m^2
$A_p = 1.7814 \times 10^{-5}$ m^2	$b = 5$ N s/m	$C_d = 0.5495$	$C_{dl} = 5.5 \times 10^{-4}$
$C_{in} = 2.649$	$C_L = 5.9 \times 10^{-6}$	$C_U = 4.2 \times 10^{-7}$	$C_{Ut} = 3.75 \times 10^{-6}$
$C_{10} = 23.2672$	$C_{20} = 1.097 \times 10^{-7}$	$k = k_{out} = k_U = k_L = 1.31$	$K = 700$ N/m
$K_L = 2.3 \times 10^{-5}$	$L = 4$	$M = 0.1491$ kg	$P_{in} = 308.2$ kPa
$P_{out0} = P_{L0} = 103.15$ kPa	$P_{U0} = 101.35$ kPa	$Q_{out0} = 3.9329 \times 10^{-4}$ m^3 s^{-1}	$V_{body} = 1.6387 \times 10^{-4}$ m^3
$V_{L0} = 3.2823 \times 10^{-4}$ m^3	$V_{U0} = 6 \times 10^{-4}$ m^3	$\rho_{out} = 0.7$ kg/m^3	$\kappa = 2.3061$

Fig. 20. Root locus for the variable b with two values of V_{U0}; □: $b = 5$ N s/m.

Changes in the upper chamber volume also affect the stability of the regulator. As this volume decreases, the system becomes more stable, as shown for the root positions when the damping $b = 5$ N s/m. At the larger volume, the system is unstable and at the smaller volume, the system is stable. This corresponds with known design goals, where the upper chamber volume must be large enough to accommodate the diaphragm diameter and travel, but is designed to be as small as possible. In addition, the oscillatory "hum" can often be induced by simply attaching a larger volume pipe to the vent discharge valve, effectively increasing the upper chamber volume.

4.2. Root locus on the diaphragm area

Another parameter that is a candidate for design change is the diaphragm area. The root locus for A_d, shown in Fig. 21, shows some interesting trends. While the root locus shows that the diaphragm could be made very small and result in stable performance of the regulator, this size diaphragm is not large enough to counteract plunger flow forces or even allow mechanical connections necessary for the physical hardware.

The remaining locus indicates that diaphragm area cannot be chosen smaller than 0.0084 m^2 in order to retain stability. Larger diaphragm areas, on the other hand, improve the response time of the system, although in the extreme, these roots also become under damped. However, because changes in diaphragm area usually imply changes in lower and upper chamber volumes, care must be taken when implementing a larger diaphragm.

4.3. Root locus on the upper chamber initial volume

The physical conditions surrounding the onset of instability include a large volume or pipe attached to the upper chamber. Often, just attaching a vent hose, common in Europe where the regulators are installed
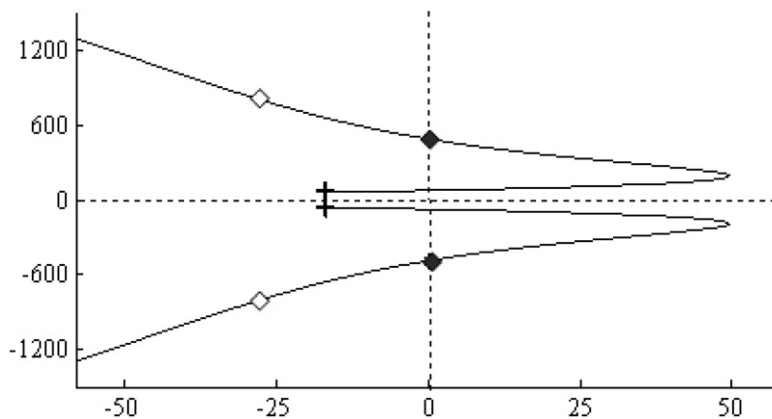

Fig. 21. Root locus on A_d; ◇: $A_d = 0.0139$ m^2 (nominal), ◆: $A_d = 0.0084$ m^2.

indoors, is enough to excite oscillations, or "humming". This indicates the need for examination of the system stability characteristics as the upper chamber volume parameter, V_{U0}, is increased. Note that the root locus shown in Fig. 22 is for the variable $1/V_{U0}$, so that origin, typically shown with an "x", is the root locations for a large upper chamber volume. In this sense, the locus in Fig. 22 is "backwards", with a larger volume pushing the root locations away from the zeros and toward the poles. A close-up view of the root locus, also seen in Fig. 22, shows that increasing V_{U0} generally decreases the system stability. The roots associated with these locations will always tend to cause under damped response, but as the upper chamber assumes values close to nominal, the response due to these roots settles quickly.

Because there are many parameters involved in the overall response, we examine another root locus for $1/V_{U0}$ in Fig. 23, which shows how the system roots are affected by changes in the upper and lower discharge
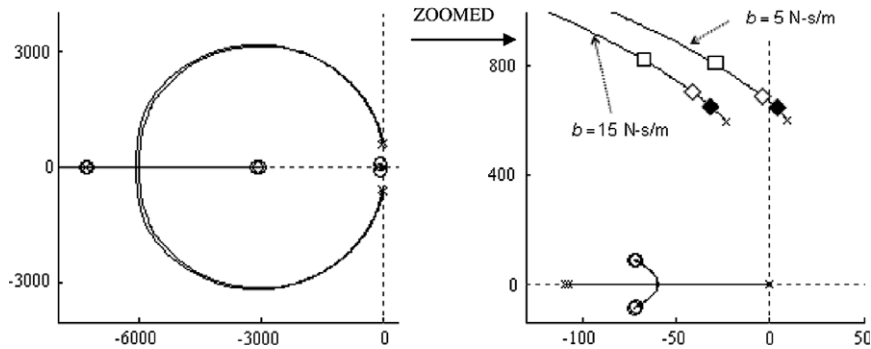

Fig. 22. Root locus on $1/V_{U0}$ with changing b; □: $V_{U0} = 6 \times 10^{-4} \, \text{m}^3$ (nominal), ◇: $V_{U0} = 12 \times 10^{-4} \, \text{m}^3$, ◆: $V_{U0} = 25 \times 10^{-4} \, \text{m}^3$.
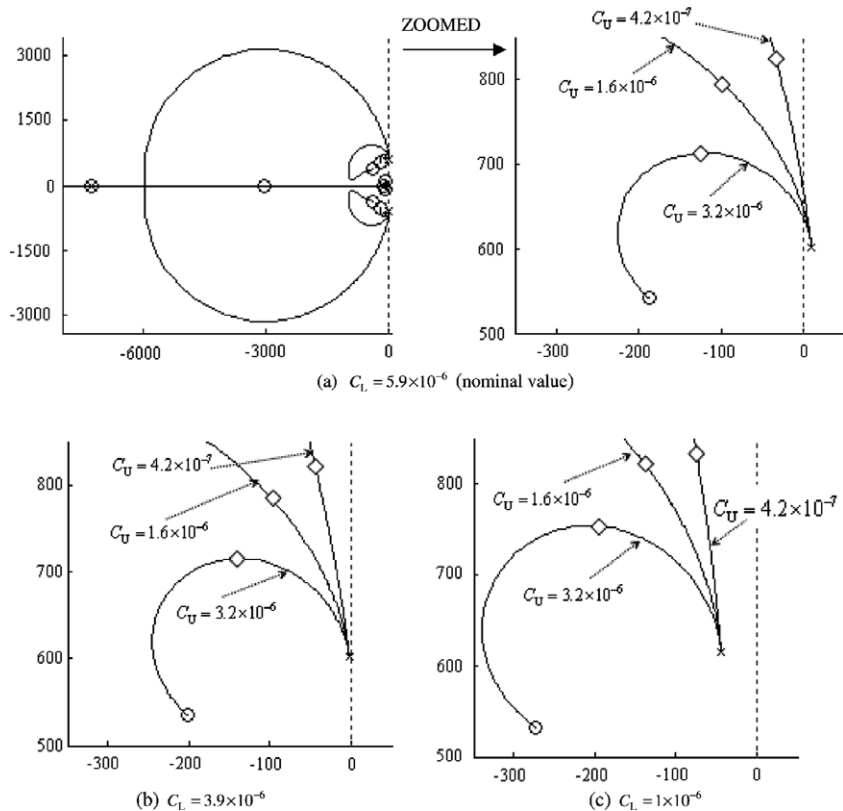

Fig. 23. Root locus for the variable $1/V_{U0}$ with changing values of C_U and C_L; ◇: $V_{U0} = 6 \times 10^{-4} \, \text{m}^3$ (nominal value).

coefficients. These coefficients are mainly a function of the hole sizes of the cap in the upper chamber, a design parameter that is relatively easy to change. The nominal values of all parameters except V_{U0} and C_U are used in Fig. 23a, where we see that increasing the upper chamber discharge coefficient, corresponding to increasing the size of the vent hole, improves stability for small upper chamber volumes but does not substantially affect stability when these volumes get large. As the lower discharge coefficient is decreased, shown in Fig. 23b and c, the entire locus tends to move away from the imaginary axis, with an associated improvement in stability. As pointed out in Fig. 22, reducing the initial size of the upper chamber still does improve the behavior of the system, but pipe and venting installations in the field will always tend to increase this volume and drive the system toward instability. Most importantly, the lower values of C_L move the root locus entirely into the stable region. This indicates that lowering the value of C_L, by reducing the associated flow area between the lower chamber and the valve body by at least a factor of two, will enhance system stability over a wide range of upper chamber volume values.

4.4. Root locus on the lower chamber initial volume

We also explore the effects of the lower chamber volume on the stability of the regulator. The root locus analysis on V_{L0} is shown in Fig. 24a. We can see that in general, changes in the lower chamber volume have only a slight effect on the system roots, causing very little change in the damping ratio and settling time. Using the general trend from Fig. 23, that decreasing the lower chamber discharge coefficient improves stability, Fig. 24b shows that decreasing C_L tends to pull the root locus into more stable regions, where "$\diamond$" indicates the location of the nominal design value of V_{L0}. This indicates that reducing the size of the flow path between the lower chamber and the body chamber tends to increase system stability.
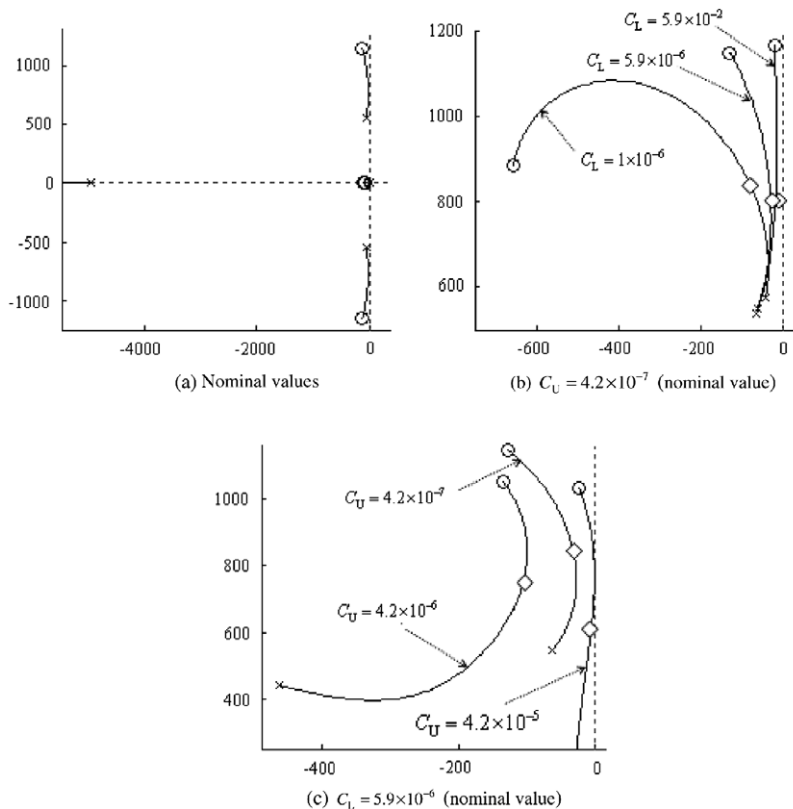

Fig. 24. Root locus for the variable $1/V_{L0}$ with changing values of C_U and C_L; $\diamond$: $V_{L0} = 3.3 \times 10^{-4}\,\mathrm{m}^3$ (nominal value).

Fig. 23 also indicates that increasing the upper discharge coefficient, C_U, may improve stability, Fig. 24c shows the locus with a the nominal value of C_L, but with a range of values for C_U, as the lower chamber volume, V_{L0}, is changed. As the upper chamber discharge coefficient is increased by a factor of ten, the locus moves toward instability. It is natural to try decreasing the value of C_U, but this change also pushes the locus toward instability.

4.5. Root locus on the upper chamber discharge coefficient

The analysis of the lower chamber volume in relation to upper and lower discharge coefficients warrants a closer look at the stability effects of these two coefficients. Fig. 25 shows the roots of the system as C_U, the flow coefficient in the upper chamber, changes for various fixed values of C_L, the discharge coefficient for flow between the lower chamber and the valve body control volumes. With C_L at the nominal value, 5.9×10^{-6}, it is clear that for both very large and very small values of C_U, the roots tend toward oscillatory or even unstable behavior. Again, this compares with the known behavior of the regulator, in that very small vent holes produce unstable oscillations, as does removing the upper chamber cover completely. Notice that as the value of C_L is decreased, which corresponds with decreasing the flow hole between the lower chamber and the body chamber, both end points of the root locus, and those in between, are pulled into the stable left half plane. This also indicates that reducing the flow area between the body and the lower chamber will enhance the stability of the regulator.

We also note that there is an optimum C_U value, located at the left-most point on the curve. Indeed, this value of C_U was a relatively constant value for a large range of C_L, and corresponds to a upper chamber vent hole about 3 times larger than the nominal size. This provides a guide for selecting the most robust value of the upper chamber discharge coefficient for all cases of the lower chamber parameter.

4.6. Dynamic simulation with improved parameters

Our root locus analysis indicates that very simple changes to the flow areas in the two chambers can have a significantly improve the performance of the regulator. In order to verify this, Fig. 26a shows the time response of the full, nonlinear simulation with changes in the upper and lower discharge coefficients. In this case, the input is a small amplitude change in outlet demand, and the response to both small and large upper chamber volumes is shown. The upper chamber flow diameter has been increased by a factor of 3, based on the root locus of Fig. 25, and the effective lower chamber flow diameter has been decreased by a factor of ten, based on the root locus of Fig. 23. Recall that with the nominal values for the flow diameters, an upper chamber volume of 0.0025 m^2 was sufficient to cause instability at low output flow rates using both the linear and nonlinear models as shown in Fig. 15a. Fig. 26 shows that these two simple changes the upper and lower discharge coefficients are sufficient to stabilize the system response for smaller output flow rates regardless of the size of the upper chamber volume.
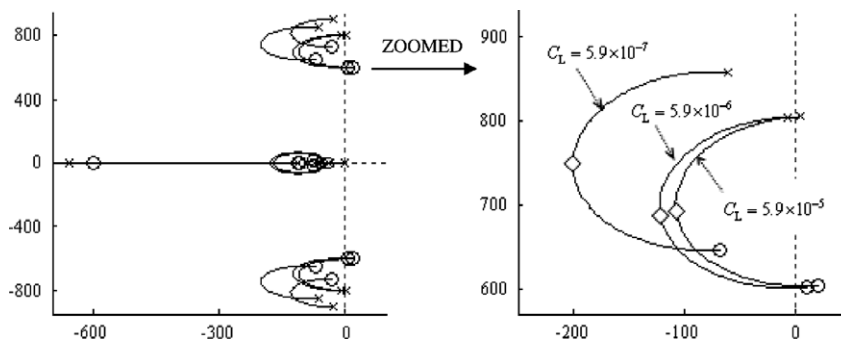

Fig. 25. Root locus on C_U with changing C_L; $\diamond$: $C_U = 3.9 \times 10^{-6}$.

(a) Small flow rate, $A = 3.2258 \times 10^{-5}$ m^2 (b) Large flow rate, $A = 4.2344 \times 10^{-4}$ m^2
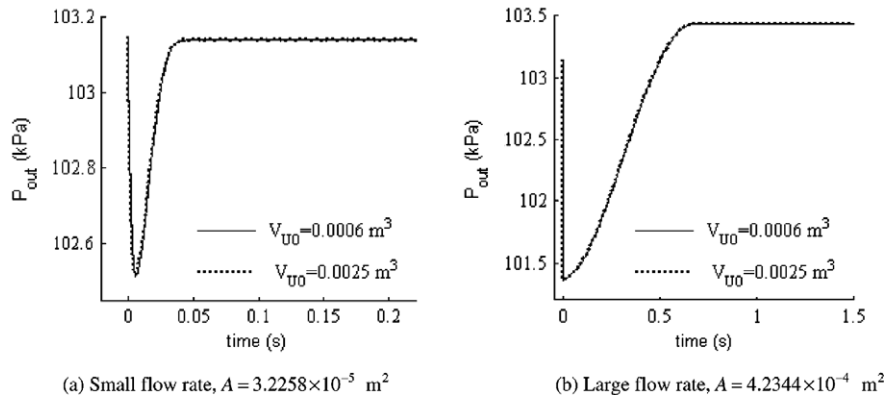
Fig. 26. Time response with changes in the upper and lower flow paths.

Larger output flow rates tend to stabilize the system as shown in Figs. 17–19. However, even at the low flow rates and with the larger upper chamber volumes, the changes in the two flow coefficients stabilize the operation of the regulator as shown if the response of Fig. 26a. Although both of these design changes ($C_{Ut} = 3.375 \times 10^{-5}$, $C_{dl} = 5.5 \times 10^{-6}$) are very easy to implement in hardware, care must be taken to allow for sufficient flow capability through the two chambers and out of the upper chamber vent hole in case the inlet flow orifice from the high pressure gas is stuck open, either though debris or mechanical failure. As noted earlier, the upper chamber vent is often a dual stage, spring loaded plate with a small discharge hole specifically for this reason.

5. Results and conclusion

This study establishes methodology to accurately model and analyze the behavior of self-regulating high pressure gas regulators. The model used has been developed from first principles to couple the mechanical and fluid system dynamics. A linear version of the model has also been developed to allow the application of root locus techniques to study the stability of the system with changes in various design parameters.

Estimation of important parameters, such as damping and discharge coefficients, was based on available steady state empirical data. Both the linear and nonlinear models produce transient and steady state responses that compared favorably with the expected behavior of the typical gas regulator. Small errors in the steady state response of the model can be attributed to the simplifying assumptions in the gas dynamics involved with the venturi effect of the flowing gas. Transient response characteristics of the linear model match the nonlinear model for small amplitude inputs, although there are significant differences in steady state values for large amplitude inputs.

One of the main reasons for the development of this model was the fact that these types of regulators tend to vibrate or hum when the relief port is connected to an extended pipe and the flow rate is kept small. This phenomenon was simulated as an increase in the upper chamber cavity on the regulator. Simulation results support the loss of stability with an increase in this volume, indicating that the model provided an accurate representation of the hardware.

In order to gain insight into the possibility of stabilizing the system through redesign, root locus techniques were used on the linear model to predict the effects of changes in various design parameters on the system response and to identify the most influential system parameters. Physical parameters that were shown to have a significant effect on stability include the damping coefficient, the diaphragm area, and upper and lower chamber volumes. Added damping, however, is difficult to control when relying on friction, may require adding hardware for accurate control, and increases the system dead-band and response time. Physical limitations on size restrict the effectiveness of changes in the sizes of the chamber volumes and the diaphragm area.

The effect of the size of the flow paths from the upper and lower chambers was also seen to have a significant effect on the system stability. Using the root locus approach, we find that reducing the size of the flow

path between the regulator body and the lower chamber provides a distinct improvement in stability. In addition, we show that there is an optimum size for the discharge hole on the upper chamber. We use the root locus techniques to show that decreasing the effective diameter of the lower chamber flow path by a factor of 10 and increasing the diameter of the upper chamber flow path by about three times theoretically improves the stability of the regulator. While there are limits on the allowable sizes for these holes, based on the discharge flow that must be allowed in the case of catastrophic failure of the regulator, we show that using these changes in the nonlinear simulation eliminates the vibration and hum and provides satisfactory performance of the regulator.

Acknowledgement

References

[1] R. Mooney, Pilot-loaded regulators: what you need to know, Gas Industr. (1989) 31–33.
[2] R. Brasilow, The basics of gas regulators, Weld. Des. Fabric. (1989) 61–65.
[3] A. Krigman, Guide to selecting pressure regulators, InTech (1984) 51–65.
[4] E. Gill, Air-loaded regulators, the smart control valve alternative, InTech (1990) 21–22.
[5] S.J. Bailey, Pressure controls 1987: sensing art challenges old technologies, Contr. Eng. (1987) 80–85.
[6] D.J. Kukulka, A. Benzoni, J.C. Mallendorf, Digital simulation of a pneumatic pressure regulator, Simulation (1994) 252–266.
[7] M. Waxman, H.A. Davis, B. Everhart, Automated pressure regulator, Rev. Sci. Instrum. (1984) 1467–1470.
[8] H.D. Bauman, Reduce pressure quietly and safely, Chem. Eng. (1992) 138–142.
[9] W.K. Ng, Measuring and reducing control valve noise pollution, I&CS (1994) 59–69.
[10] W.K. Ng, Control valve noise, ISA Trans. 33 (1994) 275–286.
[11] R.I.J. Dyck, Residential gas regulators, Pipeline Gas J. (1988) 30–33.
[12] B.G. Liptak, Pressure regulators, Chem. Eng. (1987) 69–76.
[13] M.H. Aksel, O.C. Eralp, Gas Dynamics, Prentice-Hall, Englewood Cliffs, NJ, 1994.
[14] C.A. Carmichael, Gas regulators work by equalizing opposing forces, Pipeline Gas Industr. (1996) 29–32.
[15] W.H. Seto, Theory and Practice of Mechanical Vibrations, McGraw-Hill Book Co., New York, 1964.
[16] B.T. Miralles, Preliminary considerations in the use of industrial sonic nozzles, Flow Meas. Instrum. 11 (2000) 345–350.
[17] B.B. Shannak, L. Friedel, M. Alhusein, Prediction of single- and two-phase flow contraction through a sharp-edged short orifice, Chem. Eng. Technol. 22 (10) (1999) 865–870.
[18] N. Aggarwal, N. Verma, P. Arun, Simple pendulum revisited, Eur. J. Phys. 26 (2005) 517–523.